Phase diagram and spin waves in the frustrated ferro-antiferromagnet SrZnVO(PO$_4$)$_2$

F. Landolt [1,*], Z. Yan [1], S. Gvasaliya,[1] K. Beauvois,[2] E. Ressouche,[2] J. Xu,[3,†] and A. Zheludev [1,‡]

[1]*Laboratory for Solid State Physics, ETH Zurich, 8093 Zurich, Switzerland*
[2]*Universite Grenoble Alpes, CEA, IRIG, MEM, MDN, 38000 Grenoble, France*
[3]*Helmholtz-Zentrum Berlin fur Materialien und Energie, 14109 Berlin, Germany*

Single crystals of the frustrated $S = 1/2$ ferro-antiferromagnetic proximate square lattice material SrZnVO(PO$_4$)$_2$ are studied in magnetometric, calorimetric, neutron diffraction, and inelastic neutron scattering experiments. The measured spin wave spectrum reveals a substantial degree of magnetic frustration and a large quantum renormalization of the exchange constants. The H-T magnetic phase diagram is established. It features a novel presaturation phase, which appears for only one particular field orientation. The results are discussed noting the similarities and differences with the previously studied and similarly structured Pb$_2$VO(PO$_4$)$_2$ compound.

I. INTRODUCTION

Layered vanadyl phosphates with the formula ABVO(PO$_4$)$_2$ (A,B = Sr, Zn, Pb, Ba, Cd) [1–3] have attracted considerable attention, as they realize the frustrated ferro-antiferromagnetic $S = 1/2$ Heisenberg model in an (approximate) $J_1 - J_2$ square-lattice geometry. The interest stems from theoretical predictions of exotic quantum magnetic states that may appear in such systems for either strong frustration or close to saturation in external magnetic fields. In the latter case, presaturation phases are expected to occur above the field of single-magnon Bose-Einstein condensation and below full polarization at H_{sat} [4]. Specifically, the ideal square-lattice version of the model features a quantum spin nematic phase [5–7] that is particularly robust in applied fields [4,8].

To date, unconventional presaturation phases have been identified in two species, namely BaCdVO(PO$_4$)$_2$ [9] and Pb$_2$VO(PO$_4$)$_2$ [10]. The former compound is highly frustrated [11,12] with a much reduced ordered moment in zero field [13], and a very broad presaturation phase. This phase appears in all field orientations and clearly lies above the single-magnon instability field [9,12]. All the information available to date is consistent with it being a quantum spin nematic. In contrast, quantum fluctuations in Pb$_2$VO(PO$_4$)$_2$ are much weaker, the zero-field ordered moment is quite large [14], and the presaturation phase is very narrow [10]. Whether it lies above the single-magnon condensation field is yet unclear. Unlike in BaCdVO(PO$_4$)$_2$, it appears only in magnetic fields applied perpendicular to the easy axis of weak magnetic anisotropy in this material [10]. With certainty, it is not a pure

spin nematic, as NMR experiments unambiguously show the presence of (perhaps rather complex) dipolar order and/or phase separation [10].

Is any of this behavior generic, or does it arise from the specific rather complicated and substantially different interaction geometries in the two systems? Seeking more insight into this question, we study SrZnVO(PO$_4$)$_2$, a third member of the family. It is believed to be intermediate between the above-mentioned species in terms of magnitude of frustration and the magnitude of quantum fluctuations [2,15,16]. We use inelastic neutron scattering to map out spin wave spectra in zero field and determine the relevant exchange constants. In stark contrast with Pb$_2$VO(PO$_4$)$_2$, in SrZnVO(PO$_4$)$_2$ we find a strong quantum renormalization of the spin wave energies. Neutron diffraction also reveals an ordered moment that is considerably more suppressed by quantum fluctuations than in the Pb-based compound. Nevertheless, magnetic and thermodynamic measurements that we employ to map out the H-T phase diagram uncover a narrow presaturation phase almost identical to the one seen in Pb$_2$VO(PO$_4$)$_2$ and clearly distinct from that in BaCdVO(PO$_4$)$_2$.

The crystal structure of SrZnVO(PO$_4$)$_2$ is shown in Fig. 1(a). The unit cell is orthorhombic (*Pbca*) with lattice parameters $a = 9.066(1)$Å, $b = 9.012(1)$Å, and $c = 17.513(1)$Å [17] at room temperature. The magnetism originates from $S = 1/2$ V^{4+} ions that form layers in the (a, b) plane in *approximately* a square-lattice geometry. There are eight crystallographically equivalent V^{4+} sites, four in each layer. Magnetic interactions within the layers are through V-O-P-O-V superexchange pathways and are illustrated in Fig. 1(b). Symmetry allows for two nearest-neighbor (nn) coupling constants $J_{1,1}$ and $J_{1,2}$ along the crystallographic a and b axes, respectively. There are also two distinct next-nearest-neighbor (nnn) interactions $J_{2,1}$ and $J_{2,2}$ along the diagonals of the proximate square lattice. Of the three vanadyl phosphates mentioned here, SrZnVO(PO$_4$)$_2$ appears to be the simplest one in terms of structure and the number of distinct
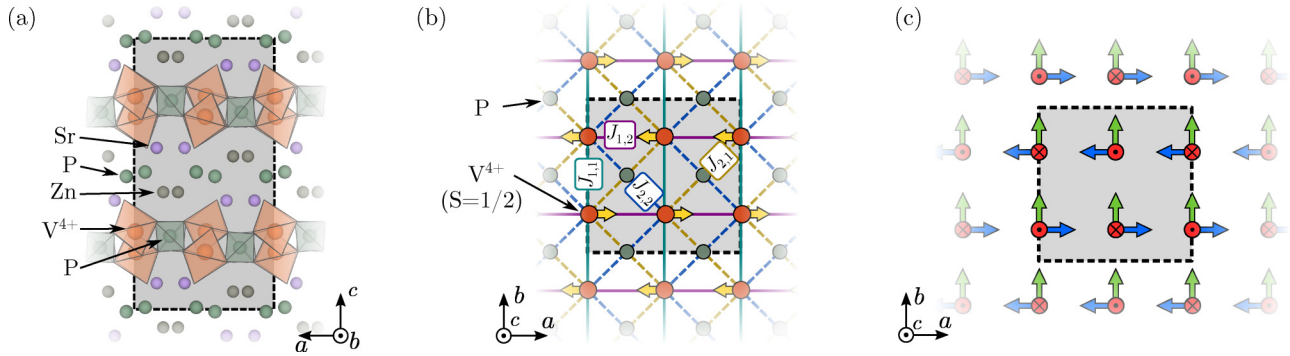
FIG. 1. Schematic view of the SrZnVO(PO$_4$)$_2$ crystal structure. (a) Projection of the entire structure onto the (a, c) plane. Shown are the VO$_6$ pyramids, the PO$_4$ tetrahedra, as well as the Sr and Zn sites. Oxygen atoms are omitted for clarity. Shaded rectangles indicate the crystallographic unit cell. (b) A single vanado-phosphate layer in the (a, b) crystallographic plane. Lines represent exchange bonds between the $S = 1/2$ V^{4+} ions, as described in the text. In the ordered phase, the magnetic structure is a columnar antiferromagnet (CAF) with spins pointing along a and alternating along b, as indicated by yellow arrows. The layers are ferromagnetically correlated along c. (c) Illustration of the V^{4+} local environment. It shows how the crystal symmetry operations transform a local quiver between the vanadium sites.

magnetic interactions. Magnetic coupling between layers is assumed to be much weaker than the in-plane one, resulting in negligible spin wave dispersion outside of the planes. This has indeed been previously confirmed by direct measurements in Pb$_2$VO(PO$_4$)$_2$ [14].

II. EXPERIMENTAL

Single crystal samples of SrZnVO(PO$_4$)$_2$ were grown by the self-flux Bridgman technique in a quartz crucible sealed under a vacuum of 10^{-4} torr. A small piece of tantalum metal was used as oxygen scavenger.

Two geometries, with the external magnetic fields applied parallel to the crystallographic a (magnetic easy axis) and c axes were explored using bulk measurements. Magnetization data were collected using a Quantum Design (QD) vibrating sample magnetometer (VSM) PPMS insert on a 6.4 mg sample. Measurements were done by scanning temperature at fixed fields. Additional field scans for fields along a were measured on a QD MPMS reciprocating sample option (RSO) using a 6.0 mg sample. A custom Faraday force magnetometer [18] PPMS insert was used to measure magnetic torque down to dilution temperatures on a 0.2 mg sample. The same sample was used in heat capacity measurements using a QD PPMS with a heat-pulse calorimeter option and a dilution refrigerator insert.

Neutron diffraction experiments were carried out on the CEA-CRG D23 lifting-counter diffractometer at ILL using neutrons with a wavelength of $\lambda = 2.35$ Å. An 80 mg single crystal sample was mounted in a dilution cryostat with the c axis vertical. Sample mosaic was 0.5°. Higher order beam contamination was suppressed using a pyrolitic graphite (PG) filter. The experiment was carried out in zero external magnetic field. The low-temperature crystal structure was refined at 10 K. The space group remains the same as at room temperature, with parameters $a = 9.07(1)$ Å, $b = 9.00(1)$ Å, and $c = 17.44(2)$ Å. Intensities of 126 structural Bragg peaks were measured in rocking scans and analyzed using FullProf [19]. The fit parameters were coordinates and isotropic thermal factor of all atoms except V (which is all but invisible to

neutrons), as well as two extinction parameters. The observed integrated intensities could be reproduced with an R factor of 5.05 (weighted R^2 factor = 6.92).

Magnetic ordering was detected by the appearance of the otherwise-forbidden (0,1,0) Bragg reflection upon cooling below $T_N = 2.6$ K. The emerging magnetic structure corresponds to a (0,0,0) propagation vector. Most magnetic Bragg peaks overlap with nuclear ones, which constitutes a formidable challenge for magnetic structure determination. The intensities of four standalone magnetic reflections were measured in complete rocking scans at $T = 50$ mK counting 1 min/point. The background (in part due to residual $\lambda/2$ beam contamination) was measured point-by-point at $T = 10$ K. For magnetic peaks that coincide with nuclear ones, a different procedure was employed. First, we measured the ratio of *peak* intensities between $T = 50$ mK and $T = 10$ K. This was done by counting 25 minutes in short incomplete rocking scans around the intensity maximum and by measuring the background at 10 K away from peak position. The thus obtained ratio was scaled by the calculated nuclear structure factor squared of this reflection, to deduce the purely magnetic contribution. Out of 65 potentially magnetic Bragg peaks we selected those for which the error bar on the magnetic structure factor squared was below 0.04 barn. The thus obtained magnetic structure factors are listed in Table I.

Inelastic neutron scattering was carried out on the cold-neutron triple axis spectrometer FLEXX at Helmholtz-Zentrum Berlin (HZB) [20]. Two crystals of total mass 867 mg were co-aligned to a cumulative mosaic of 1.8°. Sample environment was a standard "orange" cryostat with an dilution insert but no magnet was employed. Mounting the sample with c vertical enabled access to momentum transfers in the $(h, k, 0)$ reciprocal-space plane. All measurements were performed with a fixed final energy of 5 meV, a double focusing PG monochromator and horizontal focusing PG analyzer. Higher-order beam contamination was reduced by using a Be filter and a velocity selector. The measured energy resolution at the elastic position was 0.3 meV full width at half maximum. The data was collected in energy scans, typically counting 5 min per point.

TABLE I. Comparison between measured (F_{obs}^2) and calculated (F_{cal}^2) squared magnetic form factors. The first four magnetic reflections in the list are standalone; the rest are superimposed with much stronger nuclear Bragg peaks.

h	k	l	F_{obs}^2 (barn)	F_{cal}^2 (barn)
0	1	0	0.600(1)	0.588
0	−1	0	0.573(1)	0.588
0	3	0	0.351(3)	0.358
0	−3	0	0.338(3)	0.358
2	1	0	0.189(10)	0.093
1	2	−2	0.184(19)	0.075
2	3	0	0.093(16)	0.196
−3	−1	−1	0.018(10)	0
1	1	−2	0.015(10)	0
−1	−1	−1	0.002(5)	0
−2	−2	−1	0.001(10)	0
0	2	0	−0.027(11)	0
−1	−3	−1	−0.037(12)	0

III. RESULTS

A. Magnetic phase diagram

As was previously done for $Pb_2VO(PO_4)_2$ [10], measurements of magnetization vs temperature at a constant value of applied field were used to map out the magnetic phase diagram in $SrZnVO(PO_4)_2$ down to 2.1 K. The measured $M(T)$ curves for $\mathbf{H}\|\mathbf{c}$ are shown in Fig. 2 along with two representative derivative plots. Arrows indicated features associated with the onset of magnetic long range order [10]. False-color plots of the derivatives are shown in the top part of Fig. 3(a). Open blue squares indicate the phase transitions identified. Typical field scans of magnetization for fields applied along a are shown in Fig. 4(a). A sharp step is detected at 0.73 T in the ordered phase and attributed to a spin-flop transition. The inflection points of this step features are extracted by the peak position in the field derivative, shown in Fig. 4(b). The spin-flop fields are also shown in the phase diagram Fig. 3 by open blue circles.

The low-temperature-high-field sections of the phase diagram were mapped out using magnetic torque experiments. The torque signal τ was measured in field scans at fixed temperatures. Field derivatives of τ are shown in Fig. 5 and in false color plots in Figs. 3(b)–3(d). For $\mathbf{H}\|\mathbf{a}$ there appears to be a single feature (asterisk) in the data, indicative of a phase transition. We associate this feature with a transition to the fully saturated paramagnetic phase. An extrapolation of its temperature dependence to $T = 0$ yields $\mu_0 H_{\mathrm{sat},a} = 13.92$ T.

The torque signal for $\mathbf{H}\|\mathbf{c}$ shows a qualitative similar behavior above about 0.7 K. At lower temperature however, an additional feature appears at $\mu_0 H_c = 13.75$ T. The position of this new feature is almost temperature independent and becomes only sharper at lower temperatures. We associate it with the appearance of an additional presaturation phase. The second feature at full saturation retains its high temperature character and moves outside the accessible field range at low temperature. The temperature dependence of $\mu_0 H_{\mathrm{sat},c}(T)$ appears to be compatible with the previous reported saturation field of $\mu_0 H_{\mathrm{sat,powder}} = 14.2$ T determined in powder experi-
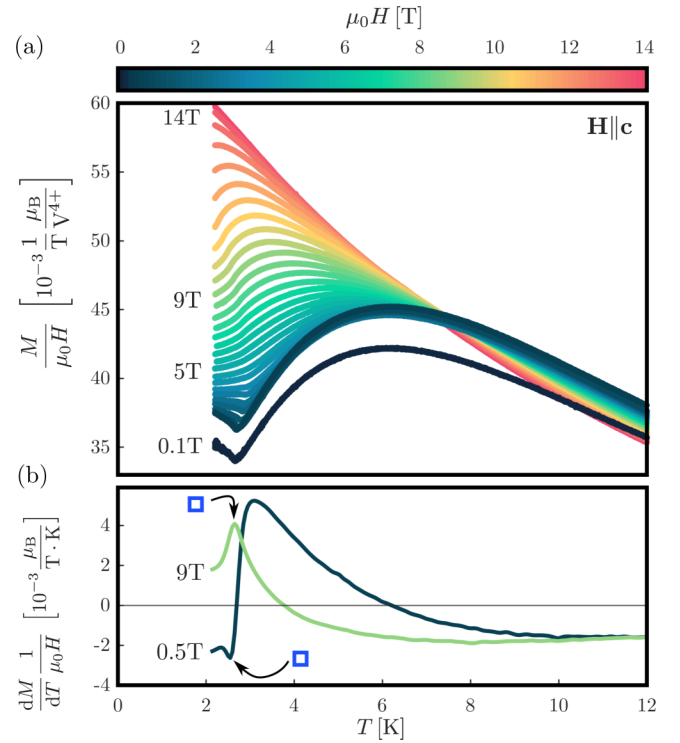

FIG. 2. (a) Magnetization data measured in temperature scans at constant fields along c. (b) Representative temperature derivatives of two magnetization scans show in (a). Extrema in the derivatives are associated with the onset of long-range magnetic order. The symbols correspond to the phase boundary points in Fig. 3(a).

ments [2]. Overall, the observed behavior of magnetization and torque in magnetic fields applied parallel or perpendicular to the anisotropy axis is remarkably similar to that previously seen in $Pb_2VO(PO_4)_2$ [10].

The accessibly low fields make it possible to confirm the phase diagram with specific heat measurements. Typical temperature scans of specific heat at constant external fields applied along c are shown in Fig. 6(a) (symbols). The boundary of the paramagnetic phase is marked by a distinct λ anomaly. Empirical power-law fits [solid lines in Fig. 6(a)] were used to determine the transition field, similar to the procedure described in Ref. [21]. Also the transition to the presaturation phase becomes visible at the lowest temperatures. As shown in Fig. 6(b), it manifests itself as a step in the measured field scans. Its magnitude decreases with increasing temperature. Above 200 mK the feature is no longer visible. The transition field was associated with the inflection point in the data and obtained by empirically function fit [solid lines in Fig. 6(b)] [22]. The resulting phase boundary data for both transitions are shown by red crosses in Fig. 3.

B. Magnetic structure

A symmetry analysis of the magnetic structure was performed following Ref. [23]. There are as many as eight different irreducible representations of the crystallographic space group assuming a (0,0,0) propagation vector. We first noted that only two of these may account for the strong magnetic (0,1,0) and (0,3,0) peaks. In turn, only one is able to
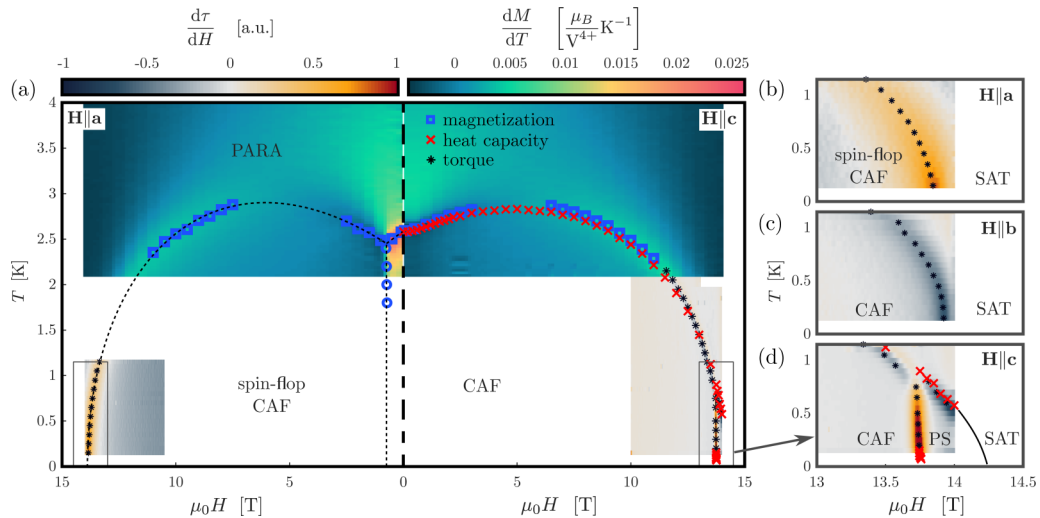
FIG. 3. Magnetic phase diagram of SrZnVO(PO$_4$)$_2$ for different field orientations. The false-color panels correspond to either temperature derivative of magnetization or the field derivative of magnetic torque. The black dashed line indicates boundaries separating the paramagnetic (PARA), columnar antiferromagnetic (CAF), and presaturation (PS) phases. Black dots, squares, and crosses are transition points determined from torque, magnetization, and specific heat data, respectively, as described in the text.

reasonably reproduce the measured intensities and explain the strong suppression of some peaks as observed experimentally. That representation is three dimensional, each basis vector corresponding to a certain pattern of spins aligned parallel or antiparallel to each of the three crystallographic axes, respectively. We find that structure factors of the measured reflections have no or only negligibly small contributions from the *b*- and *c*-axis-aligned components. We thus restrict our analysis to a single basis vector of the irreducible representation, which is a collinear CAF structure with all spins parallel or antiparallel to *a*. Within each V layer, nearest-neighboring spins along *a* are aligned parallel, while those

along *b* are antiparallel. The alignment of any two nearest-neighbor spins from adjacent layers (along the *c* axis) is parallel.

This model was assumed in the final fit to the experimental data with a single adjustable parameter, namely the magnitude of the ordered magnetic moment. We obtain
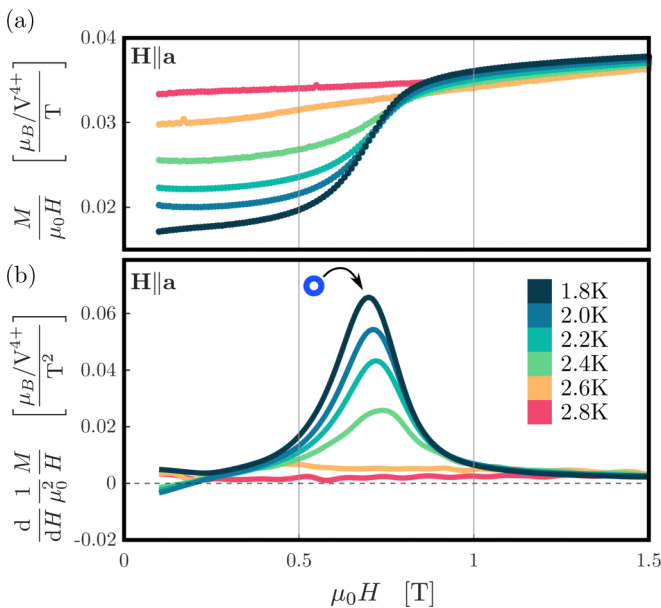

FIG. 4. (a) Field scans of magnetization normalized to field for fields parallel to *a*. The sharp increase in magnetization is attributed to a spin-flop transition. (b) Field derivatives of the data shown in (a).
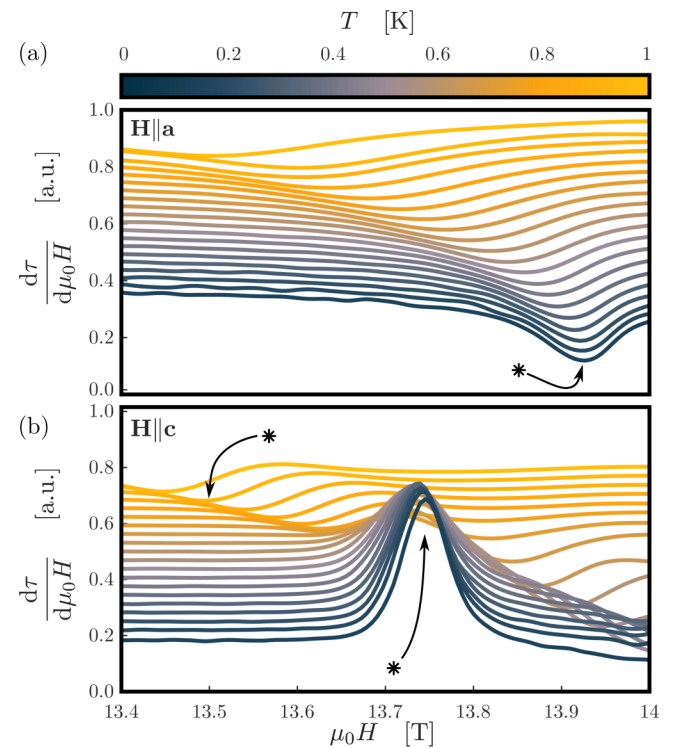

FIG. 5. Field derivatives of magnetic torque scans for two field geometries, **H**∥**a** (a) and **H**∥**c** (b). Individual curves are offset vertically to be equally spaced at 13 T for visibility. Peaks in the torque derivative are associated with phase boundaries (asterisk).
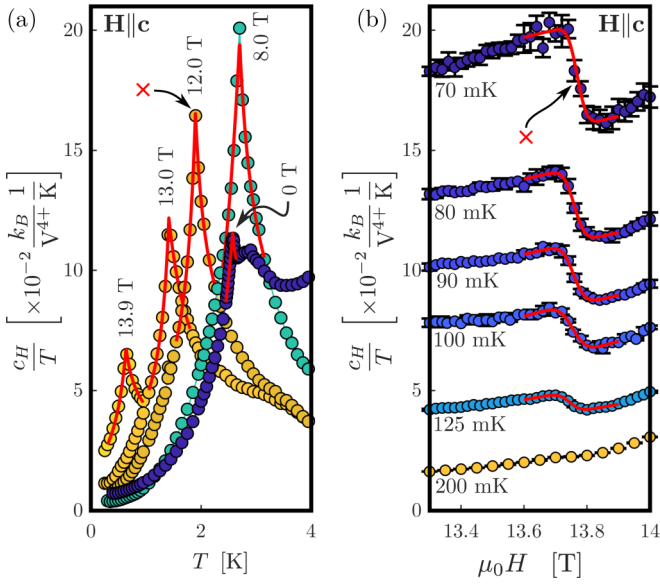
FIG. 6. Temperature scans (a) and field scans (b) of specific heat measured in SrZnVO(PO$_4$)$_2$ in magnetic fields applied along the c axis. Solid lines are empirical fits to the data to determine the corresponding transition points, as described in the text.

TABLE II. Exchange parameters obtained in a linear spin wave theory fit to the inelastic neutron spectrum measured in SrZnVO(PO$_4$)$_2$ at $T = 0.1$ K. The diagonal exchange constants are only determined up to a permutation $J_{2,1} \leftrightarrow J_{2,2}$.

$J_{1,1} = -0.35(1)$ meV	$J_{2,1} = +1.21(1)$ meV
$J_{1,2} = -0.42(1)$ meV	$J_{2,2} = +0.32(1)$ meV

ture, our quantitative estimate for m can be considered very accurate.

The estimated ordered moment is 0.367(2) μ_B smaller than previously determined in polarized-neutron experiments on powder [16]. We note, however, that the quality of those data are barely sufficient to reliably distinguish a CAF structure from a Neel state and that any normalization of magnetic intensities is based on the room-temperature crystal structure, as opposed to the actual low-temperature structure determined in the present work. We can thus be relatively certain that our single-crystal estimate is the more reliable one.

C. Spin waves

Inelastic neutron data were collected in 49 constant-Q scans for momentum transfers along several high-symmetry directions in the crystal. The cumulative data are shown in the false color intensity plot in Fig. 7. Representative scans are shown in symbols in Fig. 8. Distinct intensity peaks in the latter were attributed to scattering by spin waves. The data were modeled with linear spin wave theory (SWT), as computed using the SpinW library [24] and assuming a collinear classical CAF ground state as in Fig. 1(b). The key parameters of the model are two nn and two nnn Heisenberg exchange constants. All excitations were assumed resolution limited. The computed scattering intensities were numerically folded with the spectrometer resolution function computed in the Popovici approximation [25] using the software package ResLib [26]. The magnetic form factor for V^{4+} as well as neutron polarization factor were taken into account. The quasielastic background contribution was modeled with an empirical Lorentzian profile. The additional parameters were an overall scale factor for all scans and a flat background.
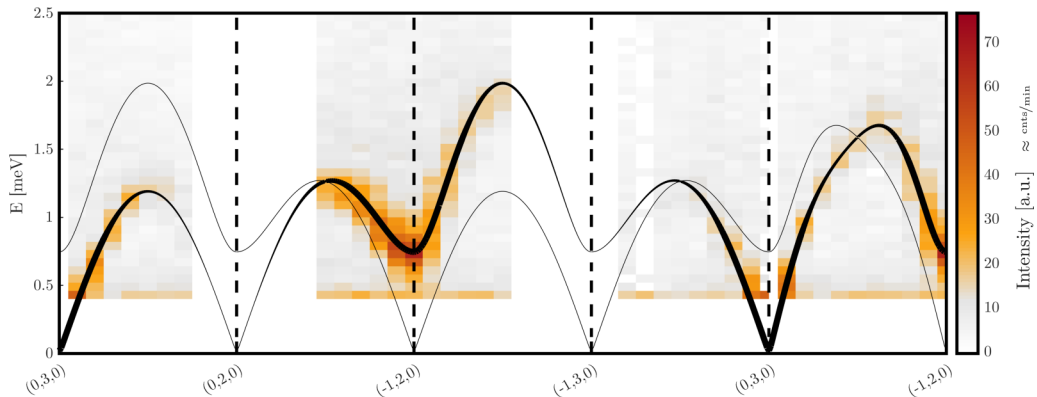
$m = 0.367(2)\ \mu_B$ per V^{4+} site. The result of the fit is tabulated in Table I for a direct comparison with experiment. While the agreement is less than perfect, and the final R factor is 18.8% (weighted $R^2 = 2.86$) which is rather large, we understand that for some reflections the statistical error bars used clearly underestimate the actual ones. Additional large systematic errors, such as those due to instrument positioning inaccuracies, can be expected due to extremely weak magnetic reflections (small ordered moment) superimposed with very strong nuclear peaks (nine entries in the lower part of Table I). Note, however, that the fitted ordered moment is primarily defined by the four standalone magnetic reflections (the first four entries) that are measured with excellent statistical accuracy and for which systematic errors are expected to be small. Under the assumption of a collinear struc-

FIG. 7. False color plot of inelastic neutron scattering intensities measured in SrZnVO(PO$_4$)$_2$ at $T = 0.1$ K. Solid lines are the spin wave dispersion calculated using the exchange couplings of Table II, as obtained in a global fit to the data. Their widths correspond to the calculated intensities.
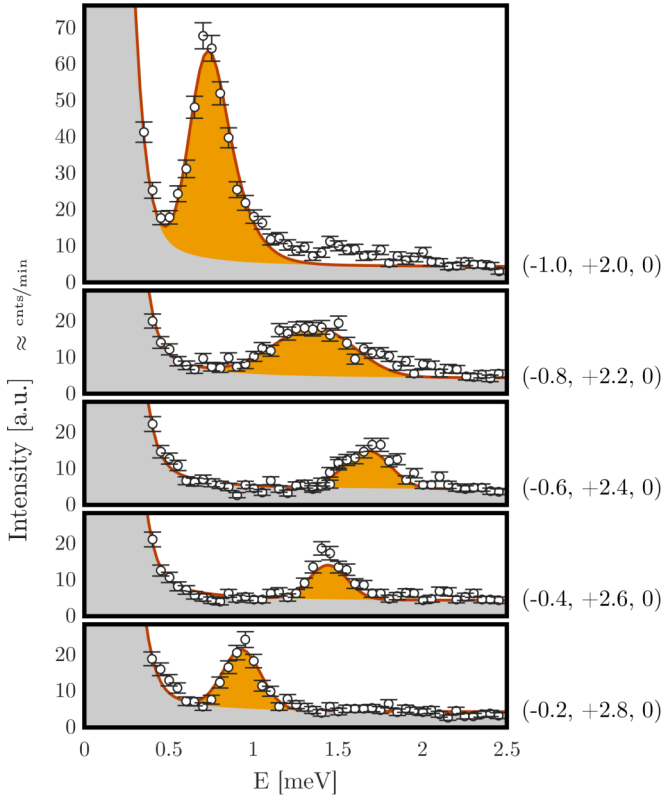
FIG. 8. Symbols: representative constant-Q inelastic neutron scattering spectra measured in SrZnVO(PO$_4$)$_2$ at $T = 0.1$ K. Shaded areas correspond to the calculated background (gray) and magnetic scattering (orange), obtained by a global fit of a spin wave model to all 49 measured scans.

All the measured energy scans were analyzed in a single global fit yielding a good agreement with $\chi^2 = 2.50$. The resulting exchange constants are tabulated in Table II. The corresponding dispersion relation is shown in solid lines in Fig. 7, with line thickness proportional to the computed intensity. Individual scans, computed using the results of the global fit, are shown in solid lines in Fig. 8. Note that there appears to be a small amount of extra intensity on the high-energy side of the spin wave peaks, not accounted for by resolution effects. We can speculate that it originates from multi-spin-wave continuum scattering. In a $S = 1/2$ system with much reduced ordered moment like SrZnVO(PO$_4$)$_2$ it is something to be expected, but only dedicated higher-resolution experiments can clarify this.

Due to the magnetic ions forming an almost-perfect undistorted rectangular lattice, distinguishing between $J_{2,1}$ and $J_{2,2}$ would only be possible by analyzing spin wave intensities at very large momentum transfers (beyond roughly the tenth Brillouin zone). From the present experiment they cannot be separated. In practice, it means that permuting the values $J_{2,1} \leftrightarrow J_{2,2}$ in Table II leads to no change in χ^2 in our fit (there are two almost identical global minima). A similar situation was encountered in the similarly structure BaCdVO(PO$_4$)$_2$ system [12]. As was the case in the latter, it is also difficult to assign the substantial differences between these two parameters to specific structural details such as bond angles.

IV. DISCUSSION

A. A comparison of the three vanadyl phosphates

The results presented above paint a very curious picture of the magnetism of SrZnVO(PO$_4$)$_2$. This material is clearly more similar to Pb$_2$VO(PO$_4$)$_2$ than to BaCdVO(PO$_4$)$_2$. Like the former and unlike the latter, it has no alternation of exchange interaction strengths along any directions [27] and correspondingly a simple columnar-antiferromagnetic ground state. Like in Pb$_2$VO(PO$_4$)$_2$, nn interactions in SrZnVO(PO$_4$)$_2$ are very similar along the main crystallographic axes, while the nnn coupling constants along the two diagonals differ by a factor of 3 to 4. The relative strength of AF interactions in SrZnVO(PO$_4$)$_2$ ($\langle J_2 \rangle / \langle J_1 \rangle = -2.0$) is not drastically smaller than in Pb$_2$VO(PO$_4$)$_2$ ($\langle J_2 \rangle / \langle J_1 \rangle = -2.9$) but much larger than in BaCdVO(PO$_4$)$_2$ ($\langle J_2 \rangle / \langle J_1 \rangle = -0.6$), where nn ferromagnetism dominates.

At the same time there are substantial differences: quantum fluctuations in SrZnVO(PO$_4$)$_2$ are much stronger than in Pb$_2$VO(PO$_4$)$_2$. It is already evident in the much suppressed value of the ordered moment in the SrZn system, which is almost as small as in BaCdVO(PO$_4$)$_2$ [13]. The same conclusion follows from the correspondence between measured SWT exchange constants in zero field and the value of the saturation field. In the fully polarized phase the single magnon instability field (a lower bound for the actual saturation field) is directly and exactly expressed through the SWT magnon energy at the ordering wave vector of the low-field structure:

$$\mu_0 H_{\text{sat}} \geqslant \mu_0 H_{\text{single-magnon}} = \frac{4S}{\mu_B g}(J_{1,1} + J_{2,1} + J_{2,2}). \quad (1)$$
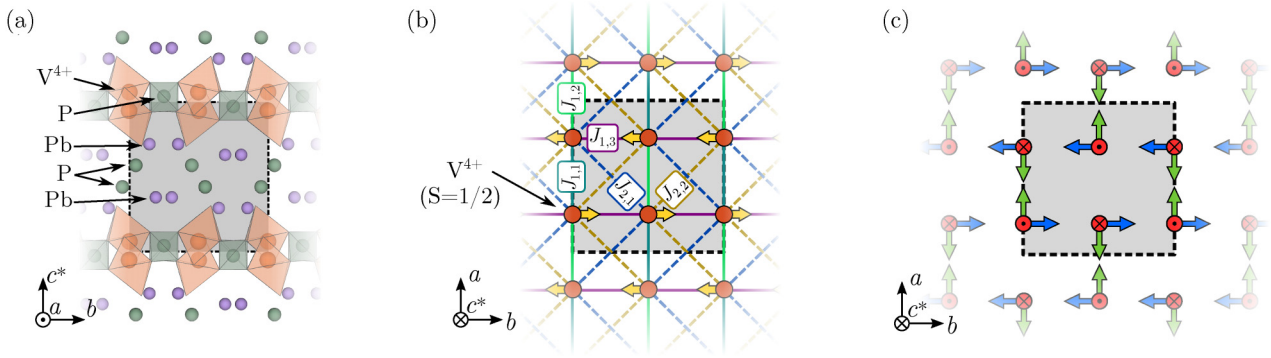
Note that the RHS expression is invariant under $J_{2,1} \leftrightarrow J_{2,2}$. Substituting the numbers in Table II gives $\mu_0 H_{\text{sat}} \geqslant 20.3$ T, by a third larger than the reported saturation field of 14.2 T [2]. This implies that the exchange constants determined in our analysis must be strongly renormalized compared to their actual values. Note that a similar computation for Pb$_2$VO(PO$_4$)$_2$ yields almost exactly the correct saturation field [2].

B. Anisotropy

In both the Pb$_2$ and SrZn systems the mysterious presaturation phase appears only for certain directions of applied field. Magnetic anisotropy is therefore crucial for either stabilizing the new phase in a particular geometry or for suppressing the phase transition in other field orientations. In these $S = 1/2$ materials two types of anisotropy need be considered: that of the g tensor and that of the exchange interactions.

1. g-tensor anisotropy

The crystal structure of SrZnVO(PO$_4$)$_2$ imposes no symmetry constrains on the V^{4+} g tensor. In fact, the VO$_6$ bipyramids within each layer are distinctly buckled, which must give rise to an anisotropic and *staggered* gyromagnetic tensor. This becomes relevant in applied magnetic fields, since it results in a staggered and potentially symmetry-breaking spin field. To analyze this effect in Figs. 1 and 9(c) we show the orientations of the local environments of V^{4+} ions within a single layer in the two materials. Each ion is represented by a quiver of three orthogonal arrows. The quivers on equivalent

FIG. 9. Same as Fig. 1, but for $Pb_2VO(PO_4)_2$.

ions are related by the corresponding crystallographic symmetry operations.

For $SrZnVO(PO_4)_2$, applying a magnetic field along c will produce a staggered spin field along the a direction. However, the $(0, \pi)$ modulation and direction of this field coincides with those of the CAF structure. A similar conclusion can be drawn for $Pb_2VO(PO_4)_2$. If, however, a magnetic field is applied along either a or b, it generates a staggered spin field along c. That staggered field is directed transverse to the zero-field CAF spin alignment. More importantly, it has a different periodicity compared to the CAF state, namely (π, π) or Néel type. We note that any additional presaturation phase transition is absent whenever this Néel field along c is present. An intriguing possibility is that it is precisely this field that destroys the presaturation state that would otherwise be manifested. This would also explain the similarity in the behavior observed in the two vanadates. A detailed theoretical study will be required to clarify this issue.

2. Exchange anisotropy

In the Moriya-Anderson superexchange mechanism, for a $S = 1/2$ system, any anisotropy of exchange interactions is due to antisymmetric Dzaloshinskii-Moriya interactions and to the so-called KSEA term, an easy axis parallel to the Dzyaloshinskii vector [28–30]. Unfortunately, the pattern of Dzyaloshinskii vectors in layered vanadyl phosphates is generally very complex. In all three materials mentioned in this work none of the in-plane bonds feature inversion centers or symmetry planes. As a result, symmetry allows for an arbitrarily oriented Dzyaloshinskii vector **D** accompanying every Heisenberg exchange constant J. The consequences of this complex microscopic picture are difficult to elucidate. The best we can do is try to at least guess the strength of this anisotropy from bulk measurements. For a classical XXZ antiferromagnet $(J_{zz} - J_{xx})/J_{xx} \sim (H_{SF}/H_{sat})^2$. Naively applying this to $SrZnVO(PO_4)_2$ gives $D/J \sim H_{SF}/H_{sat} \sim 0.05$, quite typical for a $3d$ transition metal system. The very small magnitude of this estimate ($D \sim 0.05$ meV) fully justifies our Heisenberg-model-based analysis of the spin wave spectrum measured with a typical resolution of 0.3 meV.

V. CONCLUSION

We have shown that $SrZnVO(PO_4)_2$ shows a presaturation phase similar to that in $Pb_2VO(PO_4)_2$. Qualitative and quantitative differences between the two materials suggest that this behavior may be generic. Either its origin or its suppression in certain field geometries may be related to a complex pattern of magnetic anisotropy in these compounds.

[1] R. Nath, A. A. Tsirlin, H. Rosner, and C. Geibel, Magnetic properties of $BaCdVO(PO_4)_2$: A strongly frustrated spin-$\frac{1}{2}$ square lattice close to the quantum critical regime, Phys. Rev. B **78**, 064422 (2008).

[2] A. A. Tsirlin, B. Schmidt, Y. Skourski, R. Nath, C. Geibel, and H. Rosner, Exploring the spin-$\frac{1}{2}$ frustrated square lattice model with high-field magnetization studies, Phys. Rev. B **80**, 132407 (2009).

[3] A. A. Tsirlin and H. Rosner, Extension of the spin-$\frac{1}{2}$ frustrated square lattice model: The case of layered vanadium phosphates, Phys. Rev. B **79**, 214417 (2009).

[4] H. T. Ueda and T. Momoi, Nematic phase and phase separation near saturation field in frustrated ferromagnets, Phys. Rev. B **87**, 144417 (2013).

[5] N. Shannon, T. Momoi, and P. Sindzingre, Nematic Order in Square Lattice Frustrated Ferromagnets, Phys. Rev. Lett. **96**, 027213 (2006).

[6] R. Shindou and T. Momoi, $SU(2)$ slave-boson formulation of spin nematic states in $S = \frac{1}{2}$ frustrated ferromagnets, Phys. Rev. B **80**, 064410 (2009).

[7] A. Smerald, H. T. Ueda, and N. Shannon, Theory of inelastic neutron scattering in a field-induced spin-nematic state, Phys. Rev. B **91**, 174402 (2015).

[8] H. T. Ueda, Magnetic phase diagram slightly below the saturation field in the stacked $j_1 j_2$ model in the square lattice with the jc interlayer coupling, J. Phys. Soc. Jpn. **84**, 023601 (2015).

[9] V. K. Bhartiya, K. Y. Povarov, D. Blosser, S. Bettler, Z. Yan, S. Gvasaliya, S. Raymond, E. Ressouche, K. Beauvois, J. Xu,

F. Yokaichiya, and A. Zheludev, Presaturation phase with no dipolar order in a quantum ferro-antiferromagnet, Phys. Rev. Research **1**, 033078 (2019).

[10] F. Landolt, S. Bettler, Z. Yan, S. Gvasaliya, A. Zheludev, S. Mishra, I. Sheikin, S. Krämer, M. Horvatić, A. Gazizulina, and O. Prokhnenko, Presaturation phase in the frustrated ferro-antiferromagnet $pb_2VO(PO_4)_2$, Phys. Rev. B **102**, 094414 (2020).

[11] K. Y. Povarov, V. K. Bhartiya, Z. Yan, and A. Zheludev, Thermodynamics of a frustrated quantum magnet on a square lattice, Phys. Rev. B **99**, 024413 (2019).

[12] V. K. Bhartiya, S. Hayashida, K. Y. Povarov, Z. Yan, Y. Qiu, S. Raymond, and A. Zheludev, Inelastic neutron scattering determination of the spin hamiltonian for $BaCdVO(PO_4)_2$, Phys. Rev. B **103**, 144402 (2021).

[13] M. Skoulatos, F. Rucker, G. J. Nilsen, A. Bertin, E. Pomjakushina, J. Ollivier, A. Schneidewind, R. Georgii, O. Zaharko, L. Keller, C. Rüegg, C. Pfleiderer, B. Schmidt, N. Shannon, A. Kriele, A. Senyshyn, and A. Smerald, Putative spin-nematic phase in $BaCdVO(po_4)_2$, Phys. Rev. B **100**, 014405 (2019).

[14] S. Bettler, F. Landolt, O. M. Aksoy, Z. Yan, S. Gvasaliya, Y. Qiu, E. Ressouche, K. Beauvois, S. Raymond, A. N. Ponomaryov, S. A. Zvyagin, and A. Zheludev, Magnetic structure and spin waves in the frustrated ferro-antiferromagnet $pb_2VO(PO_4)_2$, Phys. Rev. B **99**, 184437 (2019).

[15] L. Bossoni, P. Carretta, R. Nath, M. Moscardini, M. Baenitz, and C. Geibel, Nmr and μsr study of spin correlations in $srznvo(po_4)_2$: An $s = \frac{1}{2}$ frustrated magnet on a square lattice, Phys. Rev. B **83**, 014412 (2011).

[16] M. Skoulatos, J. P. Goff, C. Geibel, E. E. Kaul, R. Nath, N. Shannon, B. Schmidt, A. P. Murani, P. P. Deen, M. Enderle, and A. R. Wildes, Spin correlations and exchange in square-lattice frustrated ferromagnets, Europhys. Lett. **88**, 57005 (2009).

[17] S. Meyer, B. Mertens, and H. Müller-Buschbaum, Srzn(vo)(po4)2 and bacd(vo)(po4)2: Vanadylphosphates related but not isotypic to the bazn(vo)(po4)2 type, Z. Naturforsch. B **52**, 985 (1997).

[18] D. Blosser, L. Facheris, and A. Zheludev, Miniature capacitive faraday force magnetometer for magnetization measurements at low temperatures and high magnetic fields, Rev. Sci. Instrum. **91**, 073905 (2020).

[19] J. Rodríguez-Carvajal, Recent advances in magnetic structure determination by neutron powder diffraction, Phys. B: Condens. Matter **192**, 55 (1993).

[20] M. D. Le, D. L. Quintero-Castro, R. Toft-Petersen, F. Groitl, M. Skoulatos, K. C. Rule, and K. Habicht, Gains from the upgrade of the cold neutron triple-axis spectrometer flexx at the ber-ii reactor, Nucl. Instrum. Methods Phys. Res., Sect. A **729**, 220 (2013).

[21] D. Hüvonen, S. Zhao, M. Månsson, T. Yankova, E. Ressouche, C. Niedermayer, M. Laver, S. N. Gvasaliya, and A. Zheludev, Field-induced criticality in a gapped quantum magnet with bond disorder, Phys. Rev. B **85**, 100410(R) (2012).

[22] $c_H^{jump}(H) = A \cdot \mathrm{erf}(a \cdot (H - H_c)) + b \cdot H + c$ with free parameters A, a, H_c, b and c.

[23] A. S. Wills, A new protocol for the determination of magnetic structures using simulated annealing and representational analysis (sarah), Phys. B: Condens. Matter **276-278**, 680 (2000).

[24] S. Toth and B. Lake, Linear spin wave theory for single-q incommensurate magnetic structures, J. Phys.: Condens. Matter **27**, 166002 (2015).

[25] M. Popovici, On the resolution of slow-neutron spectrometers. IV. The triple-axis spectrometer resolution function, spatial effects included, Acta Crystallogr. Sect. A **31**, 507 (1975).

[26] A. Zheludev, Reslib resolution library for matlab, http://www.neutron.ethz.ch/research/resources/reslib (2009).

[27] $Pb_2VO(PO_4)_2$ might have a very small alternation of nn-interactions along one crystallographic direction, but the effect is not manifest in the measured spin wave spectrum.

[28] T. A. Kaplan, Single-band hubbard model with spin-orbit coupling, Z. Phys. B: Condens. Matter **49**, 313 (1983).

[29] L. Shekhtman, O. Entin-Wohlman, and A. Aharony, Moriya's Anisotropic Superexchange Interaction, Frustration, and Dzyaloshinsky's Weak Ferromagnetism, Phys. Rev. Lett. **69**, 836 (1992).

[30] L. Shekhtman, A. Aharony, and O. Entin-Wohlman, Bond-dependent symmetric and antisymmetric superexchange interactions in la_2cuo_4, Phys. Rev. B **47**, 174 (1993).